

## Relativistic and correlation effects in the photoionization dynamics of oganesson ( $Z = 118$ ): Spin-orbit-interaction-activated interchannel coupling effects

J. Jose <sup>1</sup>, S. Baral <sup>1</sup>, P. C. Deshmukh,<sup>2</sup> and S. T. Manson <sup>3</sup>

<sup>1</sup>*Department of Physics, Indian Institute of Technology Patna, Bihta 801103, Bihar, India*

<sup>2</sup>*Department of Physics, Indian Institute of Technology Tirupati, Tirupati, Andhra Pradesh 517506, India*

<sup>3</sup>*Department of Physics and Astronomy, Georgia State University, Atlanta, Georgia 30303, USA*

 (Received 21 May 2020; revised 26 June 2020; accepted 29 July 2020; published 21 August 2020)

High- $Z$  atoms are excellent laboratories to study the combination of relativistic and many-electron correlation effects in electronic structure and dynamics. In the present work, the relativistic-random-phase approximation at different levels of truncation is employed to explore the final-state correlation effects in the photoelectron dynamics of the heaviest known element in the Periodic Table: oganesson (Og) with  $Z = 118$ . The focus of this work is to illustrate the relativistic effects resulting from coupling different photoionization channels arising from spin-orbit split subshells, termed the spin-orbit-interaction-activated interchannel coupling effect. Comparison with the photoelectron dynamics of Rn on a qualitative level is also carried out, since Og is a homologue of Rn. The photoelectron dynamics of  $7p$ ,  $7s$ , and  $6d$  subshells are investigated and differences between Og and Rn, due to enhanced relativistic effects, are investigated.

DOI: [10.1103/PhysRevA.102.022813](https://doi.org/10.1103/PhysRevA.102.022813)

### I. INTRODUCTION

Unlike atoms at the low- $Z$  end of the Periodic Table, the combination of relativistic and correlation effects is crucial to the determination of the fundamental properties of superheavy elements [1]; superheavy elements do not follow completely the trends of their lighter homologues due to stronger relativistic and correlation effects [2,3]. Therefore, it is of fundamental interest to investigate the dynamics of superheavy elements both theoretically and experimentally. A contrasting study of the properties of their lighter homologues is also highly desirable to pinpoint how the increased strength of relativistic interactions alters the dynamics.

Experimental work on the electronic properties of superheavy atoms is very limited because of their very short half-lives and very low production rate. Despite these limitations, experiments have revealed properties of atoms up to Fl ( $Z = 114$ ) [4–7]. Through resonant ionization spectroscopy, the atomic structure of several high- $Z$  elements, namely Fm ( $Z = 100$ ) [8], No ( $Z = 102$ ) [9,10], and Lr ( $Z = 103$ ) [11,12], was investigated. These experimental studies stimulated sophisticated atomic calculations with higher orders of relativistic and correlation corrections included [10–12]. These measurements reveal the strong interest in the atomic properties of the superheavy elements to complete our understanding of the Periodic Table. It is, therefore, of equal interest to perform theoretical investigations, particularly for properties that are not amenable to laboratory scrutiny due to the short half-lives.

The heaviest element in the Periodic Table,  $Z = 118$ , was produced via the  $^{249}\text{Cf} + ^{48}\text{Ca}$  heavy-ion fusion reaction [13], and it was given the name oganesson (Og, E118) [14]. Its basic nuclear decay properties have been obtained experimentally [15], and the possibilities for synthesizing Og through

other fusion reactions ( $^{50}\text{Ti} + ^{248}\text{Cm}$  and  $^{54}\text{Cr} + ^{244}\text{Pu}$ ) have also been investigated [16]. However, the short lifetime of Og,  $\sim 0.89$  ms, precludes structure or dynamics experiments. Therefore, for now, these properties can only be obtained theoretically, and advanced relativistic many-body calculations are required for accuracy.

There have been a number of theoretical predictions about the electronic properties of Og with calculations of ionization potential, polarizabilities, transition probabilities, and electron affinity [17–24]. From these studies, a comparison of Og and its lighter homologue Rn suggests that the element 118 is much more active than Rn due to the enhanced spin-orbit-coupling effects [20]. For example, Og is the only rare gas that is predicted to have electron affinity [25]; the possibility of  $\text{Og}^-$  is entirely due to the stronger relativistic and correlation effects. The spectrum of dipole transitions in oganesson, including certain quantum electrodynamics (QED) corrections and the Breit interaction, was addressed by Indelicato *et al.* [26] and Lackenby *et al.* [23] and compared with Rn. All these calculations suggest that the physics of Og is rather different from that of its lighter homologues.

While discrete dipole transitions in Og have been addressed [23,26], there are as yet no reported studies of the continuum part of the oscillator strength distribution (photoionization). To remedy this situation, calculations of Og photoionization have been implemented using the relativistic-random-phase approximation (RRPA) [27] at different levels of truncation to pinpoint the final-state correlation effects. The RRPA, which is based on the Dirac equation, includes significant initial- and final-state correlation and has been quite successful in predicting the photoionization parameters of closed-shell atoms and ions [28,29]. The focus of this work is to investigate the relativistic effects in Og through

coupling of different channels arising from spin-orbit-split subshells. Specifically, spin-orbit interaction activated inter-channel coupling (SOIAC) effects have been studied for Xe, Cs, and Rn [30–32]; the coupling of channels arising from spin-orbit-split subshells in high- $Z$  atoms is expected to cause significant changes in the photoionization parameters in the near-threshold region. A comparison between the photoelectron dynamics of Rn [32,33] and Og is also examined to investigate whether or not Og is a homologue of Rn from the perspective of photoionization dynamics. The Rn results presented in this paper for comparison are taken primarily from the earlier works in Refs. [32,33]: however, we have performed additional calculations of Rn with greater energy resolution, especially near the threshold region, with the goal of unraveling the details of the SOIAC effects. Specifically, the photoionization dynamics of the  $np$ ,  $ns$ , and  $(n-1)d$  subshells of Og ( $n=7$ ) and Rn ( $n=6$ ) are investigated in this paper.

## II. THEORETICAL DETAILS

The Dirac-Hartree-Fock (DHF) orbitals  $u_i(\vec{r})$  of an  $N$ -electron atomic system satisfy [34]

$$\left( c\vec{\alpha} \cdot \vec{p} + \beta mc^2 - \frac{Z}{r} + V \right) u_i(\vec{r}) = \varepsilon_i u_i(\vec{r}), \quad i = 1, 2, \dots, N, \quad (1)$$

where  $\varepsilon_i$  is the DHF energy eigenvalue of the  $i^{\text{th}}$  orbital, and  $V$  represents the interelectron interaction term composed of direct and exchange terms defined as

$$V u_i(\vec{r}) = \sum_{j=1}^N \int \frac{d^3 r'}{|\vec{r} - \vec{r}'|} [(u_j^\dagger u_j)' u_i - (u_j^\dagger u_i)' u_j]. \quad (2)$$

It is well known that the spin of the electron makes its formal appearance with the introduction of the relativistic Dirac Hamiltonian, as opposed to the perturbative insertion of the spin-orbit interaction in the nonrelativistic Schrödinger equation. However, the presence of spin-orbit correction is not explicitly manifest in the Dirac equation; a nonrelativistic correspondence is necessary for visualizing the interaction term. The Pauli approximation was the earliest attempt to devise an approximate treatment of the Dirac equation, in which the interaction of spin angular momentum with a magnetic field was introduced [34,35]. By a series of canonical transformations on the Dirac Hamiltonian, Foldy and Wouthuysen [36,34,35] represented Dirac theory akin to the conventional nonrelativistic representation. The Foldy-Wouthuysen (FW) transformation facilitated a new Hamiltonian, a comparison of which with the nonrelativistic Hamiltonian enables us to identify the spin-orbit interaction terms in the Dirac equations as [34–36]

$$H_{\text{SO}} = -\frac{Z}{4c^2} \frac{1}{r^3} \vec{\sigma} \cdot \vec{L}, \quad (3)$$

where  $\vec{L}$  is the orbital angular momentum operator of the electron. It is not just the spin-orbit term that is evident in the FW transformation, but the relativistic mass correction, the Darwin term, etc. Dirac-Hartree-Fock theory for many-electron atoms, therefore, provides a built-in platform for dealing

with the spin-orbit interaction of electrons. The theoretical formalisms based on Dirac-Hartree-Fock equations, needless to say, are capable of unveiling  $j$ -dependent structural and dynamical properties. From a nonrelativistic correspondence perspective, the  $j$ -dependence is another way of casting the spin-orbit interaction, e.g., spin-orbit splitting of subshell thresholds. For that reason, any structural or dynamic effect concerning  $j_+ = l + s$  and  $j_- = l - s$  subshells has its formal existence in relativistic theory essentially due to the spin-orbit interaction. The SOIAC effect (details given below) is such an effect that deals with the interference effects of photoionization channels from the  $j_+$  and  $j_-$  subshells. Hence the SOIAC effect has its origin purely in the relativistic  $j$ -dependence, in particular due to the spin-orbit coupling in the nonrelativistic correspondence.

Linearized time-dependent DHF equations describe the response of an atom to an external time-dependent field:  $v_+ e^{-i\omega t} + v_- e^{i\omega t}$ . The RRPA equations can be obtained from the time-dependent DHF method given as [27,37,38]

$$\begin{aligned} (c\vec{\alpha} \cdot \vec{p} + \beta mc^2 - \frac{Z}{r} + V - \varepsilon_i \mp \omega) w_{i\pm}(\vec{r}) \\ = (v_{\pm} - V_{\pm}^{(1)}) u_i(\vec{r}) + \sum_j \lambda_{ij\pm} u_j(\vec{r}), \quad i = 1, 2, \dots, N, \end{aligned} \quad (4)$$

where the Lagrangian multipliers  $\lambda_{ij\pm}$  are incorporated to guarantee that the perturbed orbitals  $w_{i\pm}$  are orthogonal to the occupied orbitals  $u_i$ . The RRPA includes many-electron correlation effects in both initial and final states through the terms  $V_{\pm}^{(1)}$  in the above equation; all possible two-electron two-hole excitations are accounted for in the initial state and inter-channel coupling of the final-state channels, which amounts to a continuum configuration interaction. In the RRPA, the interchannel coupling effect refers to the interference effect of different continuum channels mediated via the terms in  $V_{\pm}^{(1)}$  in Eq. (4). To illustrate this coupling effect from a perturbation point of view, consider a particular photoionization channel  $|i\rangle \rightarrow |m\rangle$  represented by the perturbed transition matrix element  $\langle m | \hat{D} | i \rangle$ , where  $\hat{D}$  is the effective transition operator. The effective matrix element for  $|i\rangle \rightarrow |m\rangle$  transition inclusive of the interchannel coupling effect is written as [39,40]

$$\langle m | \hat{O}(\omega) | i \rangle = \langle m | \hat{O}(\omega) | i \rangle + \sum_{\substack{k>F \\ j\leq F}} \left[ \frac{\langle k | \hat{O}(\omega) | j \rangle \langle m j | \hat{U} | i k \rangle}{\omega - \varepsilon_k + \varepsilon_j} \right], \quad (5)$$

where  $\varepsilon_k$  and  $\varepsilon_j$  represent, respectively, the energy eigenvalues of the continuum  $|k\rangle$  and bound  $|j\rangle$  states,  $\langle m | \hat{O}(\omega) | i \rangle$  is the unperturbed matrix element in the independent-particle approximation, and  $\langle m j | \hat{U} | i k \rangle$  is the interelectronic matrix element inclusive of the exchange term, which in this context is termed the interchannel coupling matrix element. Summation over  $k > F$  and  $j \leq F$  refers to the inclusion of the effect of transitions from all  $j$  states below Fermi level ( $F$ ) to allowed  $k$  states above Fermi level ( $F$ ).

The RRPA includes all the allowed single-excitation/ionization channels from all the subshells of an atom, giving a correlated matrix element. The RRPA also allows for the possibility of truncation, which amounts to selective coupling/decoupling of the final-state photoionization channels

TABLE I. The DHF threshold energies of Og and Rn in atomic units.

Og ( $Z = 118$ )		Rn ( $Z = 86$ )	
Subshell	Energy (a.u.)	Subshell	Energy (a.u.)
$7p_{3/2}$	0.306	$6p_{3/2}$	0.38
$7p_{1/2}$	0.739	$6p_{1/2}$	0.54
$7s$	1.297	$6s$	1.07
$6d_{5/2}$	1.493	$5d_{5/2}$	2.02
$6d_{3/2}$	1.764	$5d_{3/2}$	2.19
$6p_{3/2}$	4.216	$5p_{3/2}$	5.18
$6p_{1/2}$	7.077	$5p_{1/2}$	6.41
$6s$	8.986		

accomplished by truncating the summation in Eq. (5). This convenient feature enables the study of the interchannel coupling effects of the various photoionization channels on one another; a channel in the present work refers to an allowed dipole transition from an initial state of a neutral atom to a continuum state of the photoelectron leaving the singly ionized core behind. Another important feature of the RRPA is that the calculated dipole matrix elements are gauge-invariant, i.e., length and velocity are exactly equal. While this is only approximately true for a truncated RRPA calculation, length and velocity are quite close, within a few percent, as long as all important channels are included.

The spin-orbit-interaction activated interchannel coupling (SOIAC) effect involves the coupling between photoionization channels originating from spin-orbit-split subshells, a purely relativistic effect that can only occur due to the (relativistic) spin-orbit interaction as described above. Unlike low- $Z$  atoms, the spin-orbit splitting is large in superheavy elements due to enhanced relativistic effects [17,34]. Hence, studying the photoionization dynamics of Og after selectively coupling/decoupling channels from spin-orbit-split subshells gives insight into the combined relativistic and many-body

effects in the heaviest element in the Periodic Table. Table I provides the thresholds of outer subshells of Og calculated at the DHF level [17]. For a systematic comparison, DHF thresholds of a lighter homologue of Og, namely Rn, are also provided in Table I [33]. The thresholds of spin-orbit-split valence subshells of Og,  $7p_{3/2}$ , and  $7p_{1/2}$  differ by  $\sim 12$  eV, while the  $6p_{3/2}$  and  $6p_{1/2}$  threshold split in Rn is  $\sim 4$  eV [33]. This increased relativistic splitting in Og is expected to enhance the SOIAC effect.

The objective of the present work is to investigate the SOIAC effect in Og and perform a qualitative comparison with results of Rn as a means of gauging how the enhanced relativistic effects alter the photoionization process. The levels of truncation adopted for studying the SOIAC effect in the valence subshells of Og are listed in Table II.

The 20-channel truncated RRPA calculation includes photoionization dipole channels from  $7p$ ,  $7s$ ,  $6d$ ,  $6p$ , and  $6s$  spin-orbit-split subshells (all the open channels in the range of our calculation), which is the most sophisticated calculation in the present work. The omitted channels, all closed in the  $\sim 0.3$  to 4.0 a.u. photon energy region of interest, contribute very little; this can be seen from the second term on the right in Eq. (5) in which the large energy denominator for the inner-shell channels, due to their larger threshold energies, renders the contributions of these channels quite small. In other words, the 20-channel continuum-state wave function is expanded over a sufficient number of basis functions so that no significant errors are introduced. Calculations of both cross sections,  $\sigma$ , and photoelectron angular distribution parameters,  $\beta$ , are presented in this study. Note also, only the length form of the parameters is shown in this work since the difference between length and velocity form of the matrix elements is minor, as discussed above.

### III. RESULTS AND DISCUSSION

In addition to investigating the SOIAC effect on  $7p$ ,  $7s$ , and  $6p$  photoionization parameters of Og, a qualitative

TABLE II. Channels coupled in the RRPA calculation for the study of  $7p$ ,  $7s$ , and  $6d$  subshells of Og.

Level (1): 20 channels	Level (2): 18 channels	Level (3): 14 channels
$7p_{3/2} \rightarrow \epsilon d_{5/2}, \epsilon d_{3/2}, \epsilon s_{1/2}$	$7p_{3/2} \rightarrow \epsilon d_{5/2}, \epsilon d_{3/2}, \epsilon s_{1/2}$	$7p_{3/2} \rightarrow \epsilon d_{5/2}, \epsilon d_{3/2}, \epsilon s_{1/2}$
$7p_{1/2} \rightarrow \epsilon d_{3/2}, \epsilon s_{1/2}$	$7s_{1/2} \rightarrow \epsilon p_{3/2}, \epsilon p_{1/2}$	$7p_{1/2} \rightarrow \epsilon d_{3/2}, \epsilon s_{1/2}$
$7s_{1/2} \rightarrow \epsilon p_{3/2}, \epsilon p_{1/2}$	$6d_{5/2} \rightarrow \epsilon f_{7/2}, \epsilon f_{5/2}, \epsilon p_{3/2}$	$7s_{1/2} \rightarrow \epsilon p_{3/2}, \epsilon p_{1/2}$
$6d_{5/2} \rightarrow \epsilon f_{7/2}, \epsilon f_{5/2}, \epsilon p_{3/2}$	$6d_{3/2} \rightarrow \epsilon f_{5/2}, \epsilon p_{3/2}, \epsilon p_{1/2}$	$6p_{3/2} \rightarrow \epsilon d_{5/2}, \epsilon d_{3/2}, \epsilon s_{1/2}$
$6d_{3/2} \rightarrow \epsilon f_{5/2}, \epsilon p_{3/2}, \epsilon p_{1/2}$	$6p_{3/2} \rightarrow \epsilon d_{5/2}, \epsilon d_{3/2}, \epsilon s_{1/2}$	$6p_{1/2} \rightarrow \epsilon d_{3/2}, \epsilon s_{1/2}$
$6p_{3/2} \rightarrow \epsilon d_{5/2}, \epsilon d_{3/2}, \epsilon s_{1/2}$	$6p_{1/2} \rightarrow \epsilon d_{3/2}, \epsilon s_{1/2}$	$6s_{1/2} \rightarrow \epsilon p_{3/2}, \epsilon p_{1/2}$
$6p_{1/2} \rightarrow \epsilon d_{3/2}, \epsilon s_{1/2}$	$6s_{1/2} \rightarrow \epsilon p_{3/2}, \epsilon p_{1/2}$	
$6s_{1/2} \rightarrow \epsilon p_{3/2}, \epsilon p_{1/2}$		
Level (4): 17 channels	Level (5): 17 channels	
$7p_{3/2} \rightarrow \epsilon d_{5/2}, \epsilon d_{3/2}, \epsilon s_{1/2}$	$7p_{3/2} \rightarrow \epsilon d_{5/2}, \epsilon d_{3/2}, \epsilon s_{1/2}$	
$7p_{1/2} \rightarrow \epsilon d_{3/2}, \epsilon s_{1/2}$	$7p_{1/2} \rightarrow \epsilon d_{3/2}, \epsilon s_{1/2}$	
$7s_{1/2} \rightarrow \epsilon p_{3/2}, \epsilon p_{1/2}$	$7s_{1/2} \rightarrow \epsilon p_{3/2}, \epsilon p_{1/2}$	
$6d_{5/2} \rightarrow \epsilon f_{7/2}, \epsilon f_{5/2}, \epsilon p_{3/2}$	$6d_{3/2} \rightarrow \epsilon f_{5/2}, \epsilon p_{3/2}, \epsilon p_{1/2}$	
$6p_{3/2} \rightarrow \epsilon d_{5/2}, \epsilon d_{3/2}, \epsilon s_{1/2}$	$6p_{3/2} \rightarrow \epsilon d_{5/2}, \epsilon d_{3/2}, \epsilon s_{1/2}$	
$6p_{1/2} \rightarrow \epsilon d_{3/2}, \epsilon s_{1/2}$	$6p_{1/2} \rightarrow \epsilon d_{3/2}, \epsilon s_{1/2}$	
$6s_{1/2} \rightarrow \epsilon p_{3/2}, \epsilon p_{1/2}$	$6s_{1/2} \rightarrow \epsilon p_{3/2}, \epsilon p_{1/2}$	

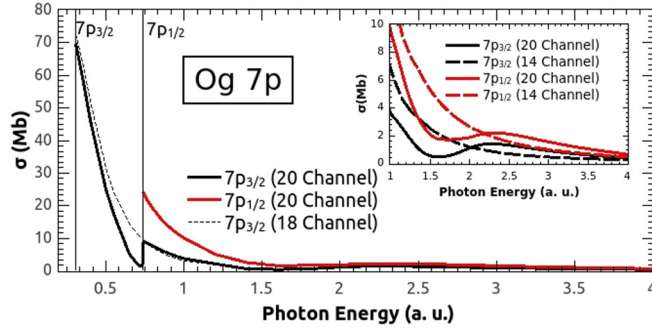


FIG. 1. Photoionization cross section for  $7p$  subshells of Og calculated in the RRP. A magnified view in the region of the Cooper minimum is shown in the inset.

comparison of these results with Rn is also made. The results are presented by subshell in each subsection. Since the  $7s$  cross section is so significantly perturbed by coupling with  $6d$  subshell channels, the analysis of  $6d$  precedes that of  $7s$ .

#### A. $7p$ subshell

Figure 1 shows the photoionization cross section for  $7p_{3/2}$  and  $7p_{1/2}$  subshells of Og at two levels of truncation. The 20-channel calculation includes all relativistic dipole-allowed single-excitation channels from  $7p$ ,  $7s$ ,  $6d$ ,  $6p$ , and  $6s$  subshells, while in the 18-channel truncated calculation, the channels from the  $7p_{1/2}$  subshell are not coupled. The  $7p$  spin-orbit splitting is  $\sim 12$  eV, due to the strength of relativistic interactions in Og. The  $7p_{3/2}$  and  $7p_{1/2}$  cross sections are rather high at the threshold of Og, and they decrease steeply with an increase in photon energy. A comparison between two levels of calculation (18 and 20 channels) showcases the interchannel coupling effect of  $7p_{1/2}$  channels on  $7p_{3/2}$ . It is seen that the effect of this interchannel coupling is significant just below the  $7p_{1/2}$  subshell threshold, where there the coupling alters the  $7p_{3/2}$  cross section markedly, generating what appears to be an induced Cooper minimum [41], a rather different SOAIC effect from what had been seen previously [30–32]. Similar effects of below-threshold interchannel coupling were noted previously in Yb  $4f$  photoionization [42], but in that case it was not a SOAIC effect. The coupling effect of continuum channels from  $7p_{1/2}$  subshells on the channels from the  $7p_{3/2}$  subshell is not very prominent. The difference between the two levels of truncation calculation is minimal above the  $7p_{1/2}$  subshell threshold, which indicates that the SOAIC effect is not very important in the  $7p_{3/2}$  cross section above the  $7p_{1/2}$  threshold. Among the three dipole channels from the  $7p_{3/2}$  subshell, the transition to  $\epsilon d_{5/2}$  is affected most strongly by the coupling with the  $7p_{1/2}$  channels.

We have also investigated the effects of channels from the  $7p_{3/2}$  subshell on those from the  $7p_{1/2}$  subshell by employing a 17-channel RRP calculation (not shown), in which channels from the  $7p_{3/2}$  were uncoupled. The resulting  $7p_{1/2}$  cross section is nearly identical to the 20-channel calculation, indicating that the effect of the  $7p_{3/2}$  subshell on the  $7p_{1/2}$  subshell is small. A Cooper minimum [41], followed by a hump, is present in both  $7p_{3/2} \rightarrow \epsilon d$  and  $7p_{1/2} \rightarrow \epsilon d$  channels at 1.4 and 1.6 a.u., respectively (evident from the

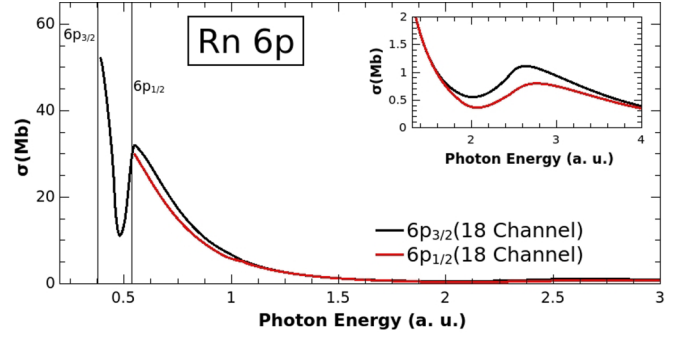


FIG. 2. Photoionization cross section for  $6p$  subshells of Rn [33]. A magnified view in the region of the Cooper minimum is shown in the inset.

inset of Fig. 1). From Table I one can see that the energy range of the Cooper minimum is the threshold region of  $6d$  subshells. To understand whether the Cooper minimum is induced due to the coupling with  $6d$  channels, the  $7p$  cross section from the 20-channel calculation is compared with that from a 14-channel calculation, in which channels from the  $6d$  subshells are uncoupled. This comparison, presented in the inset of Fig. 1, shows conclusively that the Cooper minimum is induced due to the coupling with the  $6d$  photoionization channels. This comparison demonstrates the power of truncation within the context of RRP to spotlight the specific coupling(s) responsible for a given physical effect.

To compare Og with its lighter homologue Rn, we note that photoionization of Rn  $6p$ ,  $6s$ , and  $5d$  subshells has been studied at the RRP level in Ref. [33], and in Ref. [32] the SOAIC was studied for the dipole and quadrupole photoionization parameters in Rn. The Rn  $6p$  spin-orbit splitting is  $\sim 0.1$  a.u., compared to  $\sim 0.4$  a.u. for Og  $7p$ . This difference should materially affect the interchannel coupling effects, and that is exactly what is seen. Figure 2 shows the 18-channel Rn  $6p$  cross section [33], and the gross structure is qualitatively similar to Og  $7p$ ; they are rather high at threshold and decrease steeply with energy, and in both cases there are induced Cooper minima due to coupling with channels from  $(n-1)d$  subshells. The difference between Og and Rn is that the greater spin-orbit splitting in Og allows the  $7p_{3/2}$  to drop to a much smaller value at the  $7p_{1/2}$  threshold compared to Rn. Thus, the induced minimum in the  $np_{3/2}$  cross sections is much deeper in Og as opposed to Rn below the  $np_{1/2}$  threshold. It is thus evident that the size of the spin-orbit splitting has a significant effect on the SOAIC in the region between the two thresholds.

These effects persist in the angular distribution anisotropy parameter,  $\beta$ , as well. Since the  $\beta$ 's of the  $7p_{3/2}$  and  $7p_{1/2}$  are so similar, it is convenient to calculate the weighted average for the  $7p$  subshell as

$$\beta_{7p} = \frac{\beta_{7p_{3/2}}\sigma_{7p_{3/2}} + \beta_{7p_{1/2}}\sigma_{7p_{1/2}}}{\sigma_{7p_{3/2}} + \sigma_{7p_{1/2}}}, \quad (6)$$

although below the  $7p_{1/2}$  threshold it is just the  $\beta$  for  $7p_{3/2}$ . Figure 3 shows the  $7p$   $\beta$  parameter calculated with all the 20 channels coupled. The deep dip in  $\beta$ , just below the  $7p_{1/2}$  subshell, is due to the interchannel coupling with  $7p_{1/2}$ , and

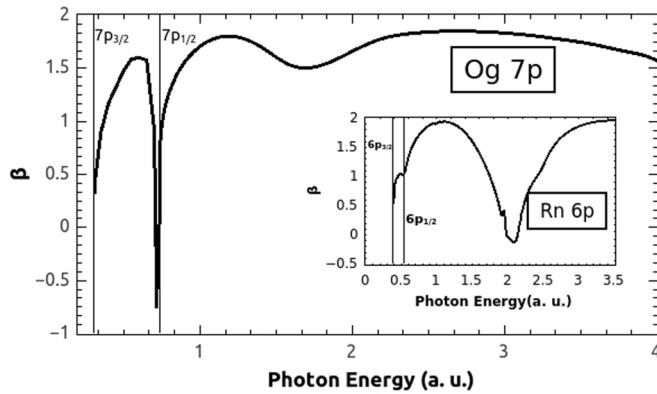


FIG. 3. Angular distribution asymmetry parameter for Og  $7p$ . The inset shows the Rn  $6p$   $\beta$  [33].

the fact that it drops down to almost  $-1$  indicates that the SOIAC effect really does induce a Cooper minimum there [43,44]. In addition, the dip at  $\sim 1.5$  a.u. is due the induced Cooper minimum due to channels from  $6d$  subshells, and the relativistic separation of the  $7p_{3/2} \rightarrow \varepsilon d$  and  $7p_{1/2} \rightarrow \varepsilon d$  minima [45] leads to a very shallow dip in  $\beta$  [43,44].

The inset of Fig. 3 shows  $\beta$  for Rn  $6p$ . The analog of the prominent dip in the Og  $\beta$  of  $7p$  due to the coupling with the  $7p_{1/2}$  subshell just below the  $7p_{1/2}$  threshold is seen as merely a kink in Rn near the  $6p_{1/2}$  subshell threshold; in other words, the dip in the Rn  $6p$  cross section is not a Cooper minimum. On the other hand, the induced minimum at about 2 a.u. is much deeper in Rn than in Og. This is because the relativistic splitting of the Cooper minima is much smaller in the Rn case. Overall, however, Rn and Og show certain gross similarities, but these are tempered by the increased strength of relativistic effects in Og, so that the details are rather different.

### B. $6d$ subshell

RRPA calculations at three levels of truncation are performed: a 20-channel truncation in which all dipole channels from  $n = 7$  and 6 subshells are included, and two 17-channel truncations in which three channels each from  $6d_{5/2}$  and  $6d_{3/2}$  are separately eliminated. Figure 4 shows the Og  $6d$  photoionization cross section from the three different calculations. As a comparison, the Rn  $5d$  cross section is presented in the inset.

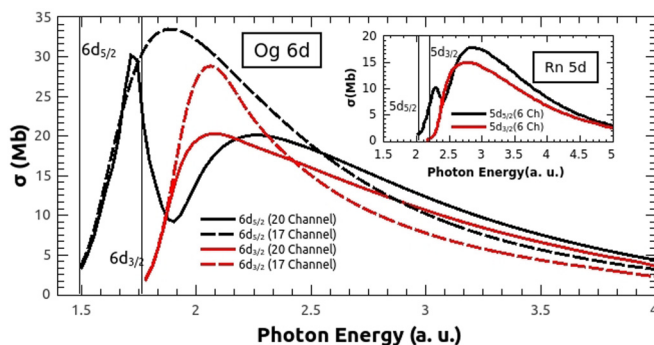


FIG. 4. Photoionization cross section of the Og  $6d$  calculated in RRPA. The inset shows the Rn  $5d$  cross section [32].

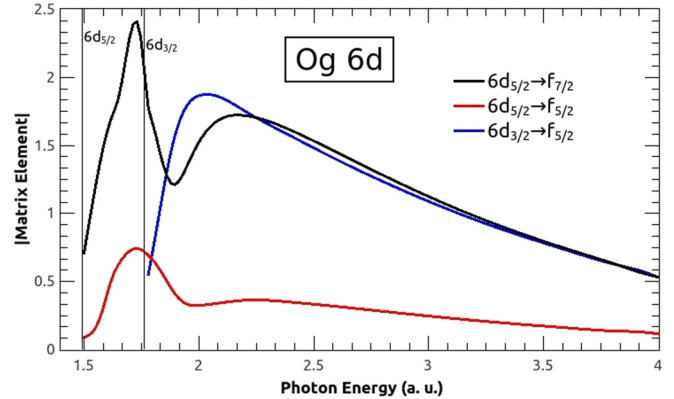


FIG. 5. Absolute value of the dipole matrix element for Og  $6d \rightarrow \varepsilon f$  transitions calculated with a 20-channel RRPA.

Interchannel coupling between photoionization channels from the spin-orbit-split  $6d_{5/2}$  and  $6d_{3/2}$  subshells influences the subshell cross section of each subshell. The  $6d_{5/2}$  (20-channel) cross section shows a bit of discontinuity just below the  $6d_{3/2}$  threshold, which is missing in the 17-channel curve (without  $6d_{3/2}$ ); this must be due to the beginning of the autoionization region. In the 17-channel coupled calculations, both  $6d_{5/2}$  and  $6d_{3/2}$  exhibit shape resonances. When the channels from the  $6d_{3/2}$  and  $6d_{5/2}$  subshells are coupled, the cross sections are broadened and lowered due to the interchannel coupling. In the  $6d_{5/2}$  cross section, there is an induced minimum due to the coupling with  $6d_{3/2}$  channels. This minimum is weaker at lower- $Z$ , where the spin-orbit splitting is much smaller. The large relativistic difference in the thresholds of  $6d_{3/2}$  and  $6d_{5/2}$  is seen to accentuate the coupling effect (SOIAC).

SOIAC in Rn  $5d$  photoionization [32] is shown in the inset of Fig. 4 for comparison. The photoionization dynamics of  $nd$  subshells are similar in nature for Rn ( $n = 5$ ) and Og ( $n = 6$ ). SOIAC is more significant in Og, as expected. The  $nd \rightarrow \varepsilon f$  transition exhibits a shape resonance in both Rn ( $n = 5$ ) and Og ( $n = 6$ ). In Og, since the spin-orbit splitting between  $6d_{5/2}$  and  $6d_{3/2}$  is larger and the coupling effect between channels from them is also enhanced, the interchannel coupling induces a pronounced minimum in the shape-resonant cross section of the  $6d_{5/2}$  subshell, whereas it is a small shoulderlike structure in Rn; in other words, the manifestation of the SOIAC effect in Og is dramatically different from that in Rn due to the increased strength of relativistic interactions in Og. To further investigate the SOIAC for Og  $6d$ , absolute values of the dominant 20-channel matrix elements  $6d_{5/2} \rightarrow \varepsilon f_{7/2}$ ,  $6d_{5/2} \rightarrow \varepsilon f_{5/2}$ , and  $6d_{3/2} \rightarrow \varepsilon f_{5/2}$  are shown in Fig. 5, where the shape resonances are seen along with the SOIAC dips in the  $6d_{5/2}$  matrix elements.

The  $\beta$  parameters for Og  $6d$  are shown in Fig. 6 along with the corresponding  $\beta$ 's for Rn  $5d$  in the inset. Comparison of the 20-channel Og results with the two truncated 17-channel  $\beta$ 's shows only minor effects of SOIAC, like the deeper dip for  $6d_{5/2}$  in the induced SOIAC minimum region. As discussed in connection with  $7p$ , the  $\beta$ 's depend on a ratio of matrix elements, so that the SOIAC effect is largely canceled out. A comparison of  $\beta$  for the  $nd$  subshells of Og ( $n = 6$ )

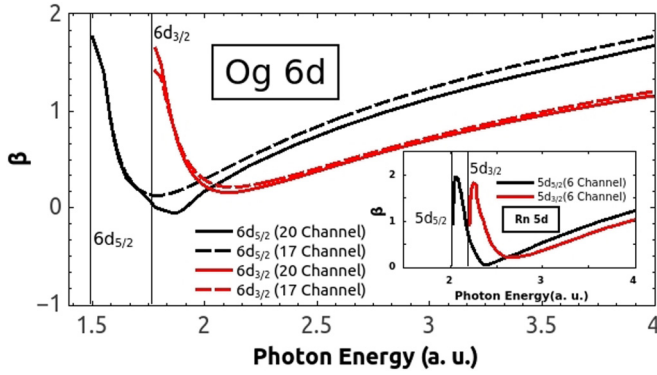


FIG. 6. Angular distribution asymmetry parameter for Og  $6d$ . The inset shows the Rn  $5d$   $\beta$  [32].

with Rn ( $n = 5$ ) shows overall a qualitative similarity between them throughout the energy range. However, close to the thresholds, the  $\beta$ 's differ qualitatively; this can be traced to a small difference in the phases of the dipole matrix elements, on which the  $\beta$ 's also depend [43,44].

### C. $7s$ subshell

For  $7s$  photoionization, a 20-channel RRPA calculation including all the single-excitation dipole channels possible from  $6s$ ,  $6p$ ,  $6d$ ,  $7s$ , and  $7p$  was performed, along with a 14-channel calculation omitting the  $6d$  channels. In addition, two 17-channel calculations, decoupling  $6d_{5/2}$  and  $6d_{3/2}$  separately, were also performed in order to ascertain the effects of each of the  $6d$  doublets individually.

Figure 7 shows the Og  $7s$  cross section at the 20- and 14-channel levels; the inset shows the analogous 18-channel Rn  $6s$  result [33] for comparison. The 14-channel  $7s$  cross section, which omits coupling with the  $6d$  channels, decreases monotonically and smoothly from threshold. However, the 20-channel result, which includes  $6d$  coupling, presents an entirely different picture, both quantitatively and qualitatively. The coupling induces a highly structured cross section; two consecutive structures (three minima) are induced, one each around the  $6d_{5/2}$  and  $6d_{3/2}$  thresholds, as seen in Fig. 7. Above these structures, there is a broad induced hump, unseen in

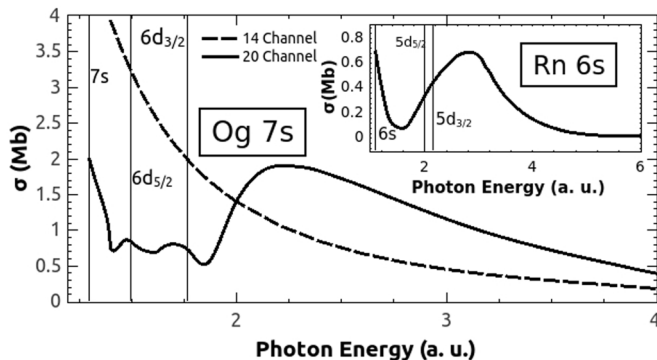


FIG. 7. Photoionization cross section for Og  $7s$  calculated in the RRPA. The inset displays the Rn  $6s$  cross section [33].

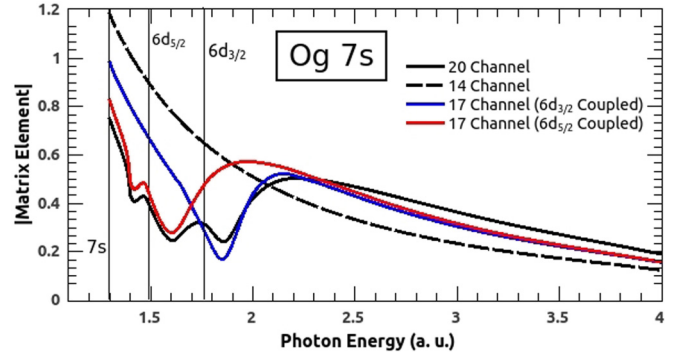


FIG. 8. Dipole matrix element of Og for the transition  $7s \rightarrow \epsilon p_{3/2}$ .

the 14-channel result, which is also caused by interchannel coupling with the  $6d$  channels.

To understand the details of this phenomenology, we investigate the coupling effects of channels from  $6d_{5/2}$  and  $6d_{3/2}$  by employing two 17-channel calculations in which channels from the respective subshells are selectively included, and we look at the  $7s \rightarrow \epsilon p_{1/2}$  and  $7s \rightarrow \epsilon p_{3/2}$  dipole channels individually. Figure 8 shows the dipole matrix element for  $7s \rightarrow \epsilon p_{3/2}$ , obtained from the 20-, 14-, and two 17-channel calculations.

When we uncouple channels from the spin-orbit-split subshells, we see dramatic effects of interchannel coupling activated through spin-orbit splitting. In the 17-channel calculation, where the effects of  $6d_{3/2}$  are uncoupled, we see multiple small structures followed by a hump in the  $7s \rightarrow \epsilon p_{3/2}$  matrix element (red curve in Fig. 8); a minimum is induced just above and just below the  $6d_{5/2}$  threshold. The minima must be due to coupling with the  $6d_{5/2}$  channels. From the other 17-channel calculation, in which the effects of channels from  $6d_{5/2}$  are uncoupled, the  $7s \rightarrow \epsilon p_{3/2}$  matrix element, shown in Fig. 8 (blue curve), decreases to a single minimum and a subsequent hump, the minimum being located above the  $6d_{3/2}$  threshold. These four sets of calculations unveil the effects of spin-orbit-split channels from the  $6d$  subshells on the  $7s \rightarrow \epsilon p_{3/2}$  transition. Channels from each spin-orbit  $6d$  subshell induce structures in the  $7s \rightarrow \epsilon p_{3/2}$  matrix element in the vicinities of their respective thresholds. To be more specific, the shape-resonant  $6d \rightarrow \epsilon f$  channels, shown in Fig. 5, adds coherently to the  $7s \rightarrow \epsilon p_{3/2}$  channel, leading to a triple minimum in the  $7s \rightarrow \epsilon p_{3/2}$  matrix element. It is evident that these distinct structures result from the size of the  $6d$  spin-orbit splitting. The spin-orbit splitting increases with  $Z$ , as relativistic effects increase,  $\sim 0.3$  a.u. in the case of Og  $6d$ . Therefore, the energetically separated photoelectron channels from these  $6d$  subshells induce structures at different locations in the  $7s \rightarrow \epsilon p_{3/2}$  matrix element, and the combined effect of all  $6d$  channels induces consecutive structures in the  $7s$  transition matrix element and cross section.

Looking now at the  $7s \rightarrow \epsilon p_{1/2}$  matrix element, shown in Fig. 9, computed in several levels of truncation (20-, 14-, and two 17-channel), the results are surprisingly different from  $7s \rightarrow \epsilon p_{3/2}$ . Even the 14-channel results, which exclude coupling with  $6d$  channels, are qualitatively different;

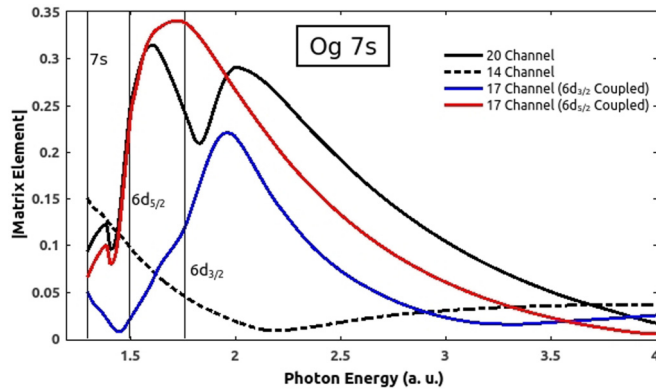


FIG. 9. Dipole matrix element of Og for the transition  $7s \rightarrow \varepsilon p_{1/2}$ .

the  $7s \rightarrow \varepsilon p_{1/2}$  matrix element exhibits a Cooper minimum, while the  $7s \rightarrow \varepsilon p_{3/2}$  does not. And the magnitude of the matrix elements is quite different in the two cases. Since the two transitions come from the same  $7s$  initial state, this means that the  $\varepsilon p_{3/2}$  and  $\varepsilon p_{1/2}$  final-state continuum wave functions are very different, and this is due to the strength of the relativistic effects in Og.

Coupling with channels from the  $6d$  subshell induces three maxima in the  $7s \rightarrow \varepsilon p_{1/2}$  matrix element, one right near threshold, and one each above the  $6d_{5/2}$  and  $6d_{3/2}$  thresholds, which is similar to the  $7s \rightarrow \varepsilon p_{3/2}$  matrix element, but the shape is quite different. To understand this in detail, in Fig. 9 the  $7s \rightarrow \varepsilon p_{1/2}$  matrix element is shown (red curve), calculated in the 17-channel truncated RRPAs in which only channels from  $6d_{5/2}$  are included and maxima are seen just above and below the  $6d_{5/2}$  threshold. Similar effects occur when the channels from the  $6d_{3/2}$  threshold alone are coupled; a hump is induced due to coupling with channels from  $6d_{3/2}$  in the  $7s \rightarrow \varepsilon p_{1/2}$  channel (blue curve). These maxima together lead to the three-maxima structure seen in the 20-channel result. In Fig. 9, due to the large  $6d$  spin-orbit separation, the maxima appear individually. It is thus clear that SOIAC effects, and their influence through interchannel coupling, are strongly mediated by relativistic effects in Og. It should also be emphasized that the structure in the Og  $7s$  cross section induced by interchannel coupling is remarkably complex, more complex than any other photoionization cross section ever reported.

To understand how these effects behave as a function of atomic number  $Z$ , Og  $7s$  is compared with Rn  $6s$  [33] in Fig. 7. For both Rn ( $n = 6$ ) and Og ( $n = 7$ ), the  $ns$  subshell cross section drops from threshold. The interchannel coupling with  $(n - 1)d$  subshell channels induces structures in the respective  $ns$  cross sections. However, an important difference is that only a simple minimum in the Rn  $6s$  cross section appears, and this is below the  $5d$  thresholds. This is in contrast with the induced structures, three minima, in the Og  $7s$  cross section, which appear over a broad energy region both below and above the  $6d$  thresholds. This is partially due to the fact that the  $ns$  and  $(n - 1)d$  thresholds are farther apart in Rn ( $n = 6$ ) in comparison with Og ( $n = 7$ ). In Og, the spin-orbit splitting between  $6d_{5/2}$  and  $6d_{3/2}$  subshells is  $\sim 0.3$  a.u., whereas in Rn, the  $5d$  splitting is around 0.17 a.u. This too contributes to the

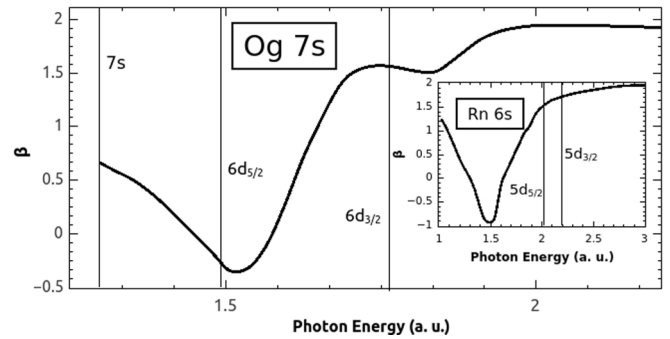


FIG. 10. Photoelectron angular distribution asymmetry parameter for the Og  $7s$  subshell. The inset shows the Rn  $6s$   $\beta$  [33].

enhanced structure in Og as compared to Rn. In other words, the Og  $7s$  cross section is quite different from Rn  $6s$ , and this is due to the increased importance of relativistic effects and how they mediate the many-body (interchannel) interactions in the high- $Z$  atom, Og.

SOIAC effects are evident as well in the angular distribution asymmetry parameter,  $\beta$ . Figure 10 shows the 20-channel Og  $7s$   $\beta$ , and the Rn  $6s$   $\beta$  resulting from an 18-channel calculation [33] is presented in the inset. For an  $s$ -subshell in a closed-shell atom,  $\beta = 2$  and is independent of energy [43], because the final-state  $\varepsilon p_{1/2}$  and  $\varepsilon p_{3/2}$  radial wave functions are exactly the same, nonrelativistically. However, as seen above, the  $7s \rightarrow \varepsilon p_{1/2}$  and  $7s \rightarrow \varepsilon p_{3/2}$  matrix elements (and, therefore, the wave functions) are very different in the two cases. Thus, we would expect a strongly energy-dependent  $\beta$ , which is exactly what is seen; the spin-orbit forces are indeed important. There are two dips in the  $7s$   $\beta$ , one each above each of the  $6d$  thresholds. Note that  $\beta$  for  $s$ -states depends essentially on the ratio of the  $\varepsilon p_{1/2}$  and  $\varepsilon p_{3/2}$  matrix elements. In this case, the near-threshold structure, seen in the  $7s \rightarrow \varepsilon p_{1/2}$  and  $7s \rightarrow \varepsilon p_{3/2}$  matrix elements (Figs. 8 and 9), cancels and it does not affect  $\beta$ . However, the other structures in the  $7s$  matrix elements are different enough that they do not cancel, resulting in the energy-dependent  $\beta$  shown in Fig. 10. Away from the  $6d$  thresholds, the  $7s$   $\beta$  moves close to the nonrelativistic value of 2.

The difference in photoelectron dynamics is exhibited in the  $ns$   $\beta$ 's of Rn ( $n = 6$ ) and Og ( $n = 7$ ); two dips are seen for Og, but only one in Rn. This comparison between the dynamics of  $ns$  photoelectrons of two elements indicates that the relativistic effects are much more significant in Og compared to Rn, which make Og dynamics significantly different from Rn.

Since there is no experiment to compare with, nor is there likely to be any time soon, it is of importance to inquire how accurate the present RRPAs are likely to be. Comparisons of RRPAs results for Xe,  $Z = 54$  [27,28] and Hg,  $Z = 80$  [46] have shown rather good agreement with experiment both qualitatively and quantitatively. Furthermore, the agreement remains about the same for both cases, thereby indicating that the RRPAs theoretical formulation does not degrade with increasing  $Z$ . This is strongly indicative that the present results are also reasonably accurate.

#### IV. CONCLUSIONS

Many-body correlation and relativistic effects in Og are investigated by exploring the photoionization of the outer  $7p$ ,  $7s$ , and  $6d$  subshells from threshold to 4 a.u. Spin-orbit splitting within the  $7p$  and  $6d$  subshells is fairly large, and this accentuates the interchannel coupling effects between channels originating from these subshells. The  $7p_{3/2}$  cross section is significantly modified below the  $7p_{1/2}$  threshold, which indicates that the SOIAC effect is significant; this demonstrates that relativistic effects are driving the system because this is a unique feature in Og, and it does not occur in its lighter homologues like Rn. The SOIAC effect in the  $6d$  subshell cross section is evident as a minimum in the  $6d_{5/2}$  cross section due to the coupling between channels from  $6d_{3/2}$  and  $6d_{5/2}$ . In the  $7s$  photoionization cross section and angular distribution parameters, the coupling with channels from  $6d_{5/2}$  and  $6d_{3/2}$  induces multiple structures. In other words, the  $7s$  cross section displays what might be termed an induced SOIAC effect. This feature is also unique to Og due to the large relativistic splitting in this superheavy element. The photoelectron dynamics of Og are qualitatively compared with that of its homologue Rn. We conclude that the photoelectron dynamics of Og are significantly different from Rn due to the enhanced relativistic effects in Og. Various features of Og photoionization, due to the relativistic effects, are simply not present in Rn. Although SOIAC exists in Rn as well, the manifestation is rather different in Og, both qualitatively and quantitatively, due to the increased strength of the relativistic forces and their mediation of the many-body electron-electron correlations, which leads to significant structure in the photoionization parameters, unlike the case of Rn. Hence, we conclude that the Og photoionization dynamics is so exotic that it is hardly a homologue of Rn from the photoelectron dynamics perspective.

It is important to reiterate that the short lifetime of Og, the heaviest element in the Periodic Table, precludes the observation of many of its atomic properties, including the present results in the laboratory, at the current level of experimental technology. At the same time, the degree of alterations in the Og photoionization due to the SOIAC effects is suggestive of the fact that similar effects could be expected in other high- $Z$  atomic systems as well; Rn dynamics itself is modified considerably due to these coupling effects, although not at

the level of Og. There are other high- $Z$  atoms, for example No ( $Z = 102$ ), where the effects of spin-orbit-split channel coupling are expected to be important. Moreover, this atom is currently intensively studied experimentally [9,10]. Therefore, the conclusions from the present results are indicative of similar effects, which could be observed from the photoionization experiments performed on any superheavy element.

The consequences of the enhanced relativistic and correlation effects on the structure and dynamics of the atom are an intriguing question. To complete our understanding of the Periodic Table, and to set the stage for the further expansion of the Periodic Table, we need to understand the properties of all of the extant elements. To fill the void in the understanding of Og, or any short-lived superheavy element for that matter, employing computational techniques is the only avenue to complete our understanding of the atomic properties of the known elements of the Periodic Table, for the time being. Although the conclusions of the present work are not expected to be verified experimentally immediately, the use of a sophisticated fully relativistic many-electron technique has enabled us to understand the key role of both relativistic and correlation effects, particularly final-state interchannel coupling effects on the photoionization parameters of Og. And given the experience using RRPA with lower- $Z$  atoms, we are reasonably sure of the general accuracy of the present results. Of course, the present results are hardly the last word. However, since the properties of Og are governed by many-electron correlation effects mediated by relativistic interactions, further inclusion of relaxation, polarization, coupling from channels from excited-bound levels, etc., which are not included in the present RRPA calculation, is not expected to modify the present results very much quantitatively, and certainly not qualitatively. In any case, the results herein represent a needed first step.

#### ACKNOWLEDGMENTS

The work of STM was supported by the US Department of Energy, Office of Science, Basic Energy Sciences under Award No. DE-FG02-03ER15428. J.J. acknowledges the support provided by SERB through Project No. ECR/2016/001564. Initial parts of the work were done when J.J. was in MCNS, Manipal University.

- 
- [1] V. Pershina and B. Fricke, *J. Chem. Phys.* **99**, 9720 (1993).
  - [2] V. G. Pershina, *Chem. Rev.* **96**, 1977 (1996).
  - [3] Y. J. Yu *et al.*, *Eur. Phys. J. D* **44**, 51 (2007).
  - [4] M. Schadel, *Angew. Chem. Int. Ed.* **45**, 368 (2006).
  - [5] A. Türler, R. Eichler, and A. Yakushev, *Nucl. Phys. A* **944**, 640 (2015).
  - [6] A. Yakushev *et al.*, *Inorg. Chem.* **53**, 1624 (2014).
  - [7] N. V. Aksenov *et al.*, *Eur. Phys. J. J.* **53**, 158 (2017).
  - [8] M. Sewtz, H. Backe, A. Dretzke, G. Kube, W. Lauth, P. Schwamb, K. Eberhardt, C. Gruning, P. Thorle, N. Trautmann *et al.*, *Phys. Rev. Lett.* **90**, 163002 (2003).
  - [9] M. Laatiaoui *et al.*, *Nature (London)* **538**, 495 (2016).
  - [10] P. Chhetri, D. Ackermann, H. Backe, M. Block, B. Cheal, C. Droese, C. E. Dullmann, J. Even, R. Ferrer, F. Giacoppo *et al.*, *Phys. Rev. Lett.* **120**, 263003 (2018).
  - [11] T. K. Sato *et al.*, *Nature (London)* **520**, 209 (2015).
  - [12] T. K. Sato *et al.*, *J. Am. Chem. Soc.* **140**, 14609 (2018).
  - [13] Yu. Ts. Oganessian, V. K. Utyonkov, Y. V. Lobanov, F. S. Abdullin, A. N. Polyakov, R. N. Sagaidak, I. V. Shirokovsky, Y. S. Tsyganov, A. A. Voinov, G. G. Gulbekian *et al.*, *Phys. Rev. C* **74**, 044602 (2006).
  - [14] P. J. Karola, R. C. Barber, B. M. Sherrill, E. Vardaci, and T. Yamazaki, *Pure Appl. Chem.* **88**, 155 (2016).

- [15] Yu. Ts. Oganessian, F. S. Abdullin, C. Alexander, J. Binder, R. A. Boll, S. N. Dmitriev, J. Ezold, K. Felker, J. M. Gostic, R. K. Grzywacz *et al.*, *Phys. Rev. Lett.* **109**, 162501 (2012).
- [16] N. Wang, E. G. Zhao, and W. Scheid, *Phys. Rev. C* **89**, 037601 (2014).
- [17] J. P. Descalux, *At. Data Nucl. Data Tables* **12**, 311 (1973).
- [18] V. Pershina, A. Borschevsky, E. Eliav, and U. Kaldor, *J. Chem. Phys.* **129**, 144106 (2008).
- [19] P. Pyykkö, *Phys. Chem. Chem. Phys.* **13**, 161 (2010).
- [20] C. S. Nash, *J. Phys. Chem. A* **109**, 3493 (2005).
- [21] I. Goidenko, L. Labzowsky, E. Eliav, U. Kaldor, and P. Pyykkö, *Phys. Rev. A* **67**, 020102(R) (2003).
- [22] K. S. Pitzer, *J. Chem. Soc. Chem. Commun.*, 760b (1975).
- [23] B. G. C. Lackenby, V. A. Dzuba, and V. V. Flambaum, *Phys. Rev. A* **98**, 042512 (2018).
- [24] B. Fricke and G. Soff, *At. Data Nucl. Data Tables* **19**, 83 (1977).
- [25] E. Eliav, U. Kaldor, Y. Ishikawa, and P. Pyykkö, *Phys. Rev. Lett.* **77**, 5350 (1996).
- [26] P. Indelicato, J. P. Santos, S. Boucard, and J. P. Desclaux, *Eur. Phys. J. D* **45**, 155 (2007).
- [27] W. R. Johnson and C. D. Lin, *Phys. Rev. A* **20**, 964 (1979).
- [28] W. R. Johnson and K. T. Cheng, *Phys. Rev. A* **20**, 978 (1979).
- [29] S. Saha, J. Jose, P. C. Deshmukh, G. Aravind, V. K. Dolmatov, A. S. Kheifets, and S. T. Manson, *Phys. Rev. A* **99**, 043407 (2019).
- [30] M. Ya. Amusia, L. V. Chernysheva, S. T. Manson, A. M. Msezane, and V. Radojević, *Phys. Rev. Lett.* **88**, 093002 (2002).
- [31] H. Farrokhpouret *et al.*, *J. Phys. B* **39**, 765 (2006).
- [32] S. S. Kumar, T. Banerjee, P. C. Deshmukh, and S. T. Manson, *Phys. Rev. A* **79**, 043401 (2009).
- [33] P. C. Deshmukh, V. Radojevic, and S. T. Manson, *Phys. Rev. A* **45**, 6339 (1992).
- [34] I. P. Grant, *Relativistic Quantum Theory of Atoms and Molecules: Theory and Computation* (Springer, 2010).
- [35] J. D. Bjorken and S. D. Drell, *Relativistic Quantum Mechanics* (McGraw-Hill, New York, 1964).
- [36] L. L. Foldy and S. A. Wouthuysen, *Phys. Rev.* **78**, 29 (1950).
- [37] A. Dalgarno and G. A. Victor, *Proc. R. Soc. London, Ser. A* **291**, 291 (1966).
- [38] W. R. Johnson, C. D. Lin, K. T. Cheng, and C. M. Lee, *Phys. Scr.* **21**, 409 (1980).
- [39] M. Ya. Amusia, *Atomic Photoeffect* (Pergamon, Oxford, 1990).
- [40] E. W. B. Dias *et al.*, *Phys. Rev. Lett.* **78**, 4553 (1997).
- [41] M. Kutzner and V. Radojević, *Phys. Rev. A* **49**, 2574 (1994).
- [42] J. W. Cooper, *Phys. Rev.* **128**, 681 (1962).
- [43] T. E. H. Walker and J. T. Weber, *Phys. Rev. Lett.* **30**, 307 (1973).
- [44] S. T. Manson and A. F. Starace, *Rev. Mod. Phys.* **54**, 389 (1982).
- [45] Y. S. Kim, A. Ron, R. H. Pratt, B. R. Tambe, and S. T. Manson, *Phys. Rev. Lett.* **46**, 1326 (1981).
- [46] W. R. Johnson, V. Radojević, P. Deshmukh, and K. T. Cheng, *Phys. Rev. A* **25**, 337 (1982).